# Computational Fluid Dynamic of Geothermal Membrane Distillation

C. Rivera[1], C. Sanchez[1], M. Troyer[1], J. Paiz[1], F. Huang Ph.D. [1]
1. Environmental Engineering Department, New Mexico Institute of Mining and Technology, Socorro, NM, USA

## Introduction

Membrane distillation (MD is an emerging water desalination technique proposed as an alternative or supplement to reverse osmosis (RO). RO is a very effective treatment process, but is particularly energy intensive due to its principle mechanism: high pressure is applied against the natural osmotic pressure in order to force water across a nonporous membrane. Due to the high pressure of the system, a dense layer of solids or precipitates develops on the membrane. The membrane eventually fouls, rendering it inoperable. The high energy input required by RO, as well as the cost associated with replacing fouled membranes, has led to many investigations of other treatment methods over the last thirty years. The limiting factor in these investigations has been the characteristics of the membrane. MD is a separation process that relies on vapor pressure gradient to drive the production of purified water across a hydrophobic membrane. In direct contact membrane distillation (DCMD), both the hot water and cold permeate are in direct contact with the membrane. The temperature difference across the membrane induces the vapor pressure gradient. Theoretically, this technology has cost advantages over RO because it is a low-pressure system and may have less membrane fouling potential.

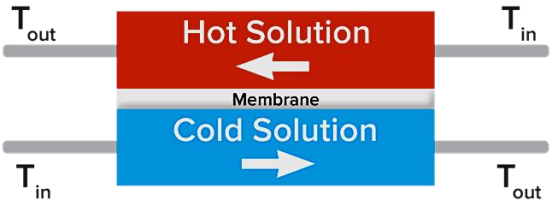


**Figure 1**. Water flow across the membrane

These numerous advantages of DCMD make it a justifiable endeavor to model a heat and mass transfer computation fluid dynamic (CFD) model to guide the design and operation of experimental DCMD investigations.

A 3-D COMSOL® model was established for a hollow fiber membrane (HFM) module for direct contact membrane distillation (DCMD). Postprocessing results evaluated the membrane flux and temperature polarization coefficient as a function of packing density of the modules, packing configuration, shell-side flow rates, and correlated the experimental data with the model predictions.

## Theory

A hollow fiber DCMD process relies on momentum, heat, and mass transfer between the feed, membrane, and permeate domains. In the process, the velocity of the feed water on the shell side delivers the hot water to the membrane boundary. The cold-permeate flowing on the lumen side of the membrane establishes a vapor pressure gradient across the membrane, making it energetically favorable for water to vaporize, and diffuse through the membrane. The rate of vapor diffusion through the membrane is restricted by the amount of pore space in the membrane, the pore size, and the tortuosity of the path it must travel. When the vapor molecule reaches the other side of the membrane, it will condense and is swept up by the flow of the permeate. The heat transfer across the membrane is mainly due to conduction through the membrane material, stagnant air, and water vapor. Evaporation of the water causes heat loss along the membrane boundary on the feed side, contributing to a thermal boundary layer at the membrane, which compounds along the length of the membrane. Likewise, the condensation on the permeate side of the membrane releases heat, establishing a thermal boundary layer on the permeate side. As the vapor molecule diffuses through the pores of the membrane, it will contact the membrane material, and other molecules, losing energy, and moving towards thermal equilibrium with its surroundings.

## Experimental Set-up

The main objective was to design three-dimensional computational fluid dynamic, heat transfer and mass models in order to optimize the flow rate and packing density of the membrane modules. The CFD simulations for this research project utilized a finite element CFD software program, COMSOL Multiphysics®. The physics used in this model coupled flow, heat transfer, and the transport of diluted species to simulate similar conditions applied to the bench-scale DCMD modules. The model geometry was based on the bench-scale DCMD modules that

were employed for the validation experiments. The cylindrical coordinate system was applied for the physics in the simulations.

Six geometries were employed, which included three different packing densities, and two configurations. One configuration assumed the center of each membrane has a distance (d) of 1 mm from the center of adjacent membranes, and is referred to in this paper as set distance (SD). The second attempts to spread the membranes as evenly as possible throughout the module area, recognizing that wall interference occurs, and is referred to as equally spaced (ES). A diagram of the simulated module geometry is shown in Figure 2. The specifications of the experimental module and membrane geometries are summarized in Table 1 for the cylindrical system. The packing densities and associated number of fibers are shown in Table 2. All simulations had a feed inlet temperature of 70℃ and permeate inlet temperature of 20℃. A summary of the varied parameters for CFD investigations is shown in Table 3. The geometry of the simulated modules can be visualized in Figure 3.

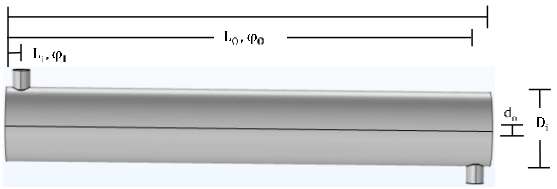

**Figure 2**. Simulated module geometry.

**Table 1**. Geometry specifications

| Parameter | Variable | Value |
|---|---|---|
| Module length | L | 6.6 cm |
| Module inner diameter | $D_i$ | 1.27 cm |
| Inlet/Outlet inner diameter | $D_o$ | 0.3175 cm |
| Inlet z- position | $L_I$ | 0.2 cm |
| Outlet z-position | $L_O$ | 6.4 cm |
| Inlet φ-position | $\varphi_I$ | 0° |
| Outlet φ -position | $\varphi_O$ | 180° |
| Inner diameter of membrane | $d_i$ | 595µm |
| Outer diameter of membrane | $d_o$ | 810µm |

**Table 2**. Packing densities

| Packing density | Number of fibers |
|---|---|
| 14.6% | 7 |
| 27.1% | 13 |
| 39.8% | 19 |

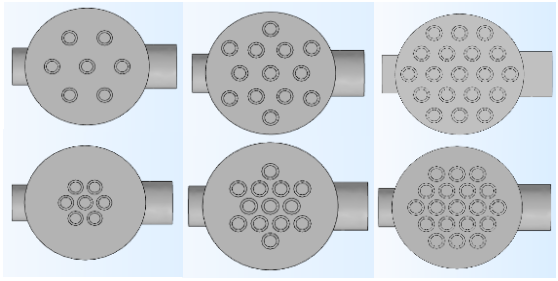

**Figure 3**. Simulated module geometry.

**Table 3. S**imulation study summary

| Number of membranes | Distribution | Feed flow rate (mL/min) |
|---|---|---|
| 7 | SD | 30/ 60/ 120/ 180/ 240 |
| | ES | 30/ 60/ 120/ 180/ 240 |
| 13 | SD | 30/ 60/ 120/ 180/ 240 |
| | ES | 30/ 60/ 120/ 180/ 240 |
| 19 | SD | 30/ 60/ 120/ 180/ 240 |
| | ES | 30/ 60/ 120/ 180/ 240 |

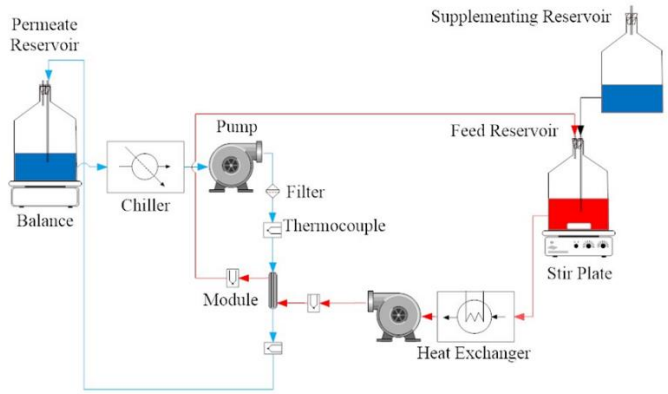


**Figure 4**. Diagram of experimental setup

A lab-scale DCMD system was constructed for validation tests. In figure 4 the lab-scale set-up is shown. The performance of the DCMD system was evaluated at the hot-side inlet temperature of about

70°C and the cold-side inlet temperature of about 20°C.

Permeate water fluxes were calculated using the recorded data. The slope of the cumulative mass versus time curve represented the permeate production rate and was used to estimate the water flux (liters/m$^2$-hour, LMH) of the module at a specific temperature gradient:

$$Water\ flux\ (LMH) = \frac{\dot{M}\rho_w}{A_f}$$

where Ṁ is the mass accumulation rate of water (kg/hour) in the permeate reservoir, $\rho_w$ is the density of water at 20°C (1 kg/L), and $A_f$ is total external surface area (m$^2$) of the hollow fiber membranes in the module.

## Governing Equations

The equations in Table 4 describe steady state, incompressible, non-isothermal laminar flow, with mass transport of vapor across the membrane. These transport equations were incorporated for the simulations, which assume steady state conditions. $\nabla$ represents the del operator, $\boldsymbol{u}$ is the velocity vector, $p$ is dynamic pressure, $\boldsymbol{I}$ is the unit tensor, $\mu$ is the dynamic viscosity, $(\nabla)^T$ is the transpose of del operator, $\boldsymbol{F}$ is a volume force vector, $C_p$ is the specific heat of a fluid, $Q$ is a heat source, $\boldsymbol{q}$ is heat flux, $k$ is thermal conductivity coefficient, $D$ is the diffusion coefficient, $c$ is concentration, $\boldsymbol{N}$ is molar flux, and $R$ is a production or consumption rate (COMSOL Multiphysics® User Guide). Table 5 shows the boundary conditions applied to the model.

**Table 4**. Transport equations for momentum, energy, and mass transport.

| Transport type | Transport equation |
|---|---|
| Continuity | $\nabla \cdot (\rho \boldsymbol{u}) = 0$ |
| Momentum | $\rho(\boldsymbol{u} \cdot \nabla \boldsymbol{u}) = \nabla \cdot [-p\boldsymbol{I} + \mu(\nabla \boldsymbol{u} + (\nabla)^T] + \boldsymbol{F}$<br>$\rho\, \nabla \cdot \boldsymbol{u} = 0$ |
| Energy in fluid | $\rho C_p \boldsymbol{u} \cdot \nabla T + \nabla \cdot \boldsymbol{q} = Q$<br>$\boldsymbol{q} = -k\nabla T$ |
| Energy through membrane | $\nabla \cdot \boldsymbol{q} = Q$<br>$\boldsymbol{q} = -k\nabla T$ |
| Mass | $\nabla \cdot (-D_i \nabla c_i) = R_i$<br>$\boldsymbol{N_i} = -D_i \nabla c_i$ |

Knudsen-molecular transition was found to be the dominant diffusion method. The molar flux for the Knudsen-molecular transition region was fit to a simple Fick's diffusion model for integration with the CFD simulation.

$$N = -D\nabla c$$
$$N = B_M\left(p^o_{w,fm} - p^o_{w,pm}\right)$$
$$= -\frac{1}{RT_m}\left(\frac{D^k_w D^0_{w-a}}{D^0_{w-a} + p_a D^k_w}\right)\left(\frac{-\Delta p_w}{\delta}\right)$$
$$\nabla c = -\Delta c = -\frac{\Delta p^o}{\delta R T_i}$$
$$D = \left(\frac{D^k_w D^0_{w-a}}{D^0_{w-a} + p_a D^k_w}\right)$$

The vapor concentration at the water-air interface of the membrane on the feed side was determined by the local vapor pressure and temperature at the membrane boundary:

$$c_{fm} = \frac{p^o_w}{RT}$$

Likewise, the concentration at the water-air interface of the membrane on the permeate side was determined by the local vapor pressure and temperature at the membrane boundary:

$$c_{pm} = \frac{p^o_w}{RT}$$

The evaporation at the water-air interface of the membrane on the feed side caused a boundary heat flux:

$$q_{fm} = -H_{vap} * N = -H_{vap} * \lambda_{c_{fm}}$$

Similarly, the condensation at the water-air interface of the permeate side at the membrane caused a heat flux:

$$q_{pm} = H_{cond} * N = -H_{cond} * \lambda_{c_{pm}}$$

where $\lambda_c$ is the Lagrange multiplier of the concentration, which corresponds to the flux. A weak constraint was applied to this boundary condition in order to create the Lagrange multiplier.

**Table 5**. Boundary conditions

| Boundary | Boundary condition | Value |
|---|---|---|
| Feed inlet | Momentum: Mass flow rate | m_30/ m_60/ m_120 /m_180/ m_280 |
| | Energy: Temperature | $T_{feed}$ |
| Permeate inlet | Momentum: Laminar inflow, $u_{ave}$ | 0.35965 m/s |
| | Energy: Temperature | $T_{perm}$ |
| Feed outlet | Momentum: Pressure outlet | 101325 Pa |
| | Energy: Outflow | NA |
| Permeate outlet | Pressure outlet | 101325 Pa |
| | Energy: Outflow | NA |

## Experimental and Simulation Results

The membrane parameters used as model inputs were measured values with the exception of tortuosity, which was assumed to be a value between one and two. This parameter was allowed to fluctuate until the lab test data fit between the ES and SD predictions. The results shown were simulated with a value of 1.75 for membrane tortuosity. The bulk temperature values, $T_{fb}$ and $T_{pb}$, used to calculate the TPC from simulations were found by averaging the temperature in each bulk fluid volume. The temperature of the membrane surface of the feed side, $T_{fm}$, and the membrane surface on the permeate side, $T_{pm}$, were found by averaging the temperature along at each respective interface for all membranes in a simulated module. The individual lab tests were averaged, and the standard error corresponding to a 95% confidence interval for each average is displayed on the charts in this section as error bars.

### Entrance and exit effects

Including the entrance and exit effects in the CFD simulations significantly increases the computational burden. Efforts were made to examine whether these effects could be ignored in order to reduce the duration of CFD computation time. The entrance and exit effects on the shell side are dictated by the inlet and outlet diameter, the flow rate of the water entering the module, the number and position of membranes that the incoming velocity vectors come into contact with, as well as the length of the module. The entrance effects varied for the different geometries. The laminar velocity assumption held true throughout the investigations. The higher velocity entering the inlet led to higher velocity near the module wall opposite the inlet, and decreased velocity near the shell wall immediately downstream from the inlet. Likewise, the flow just upstream of the outlet increased, while the flow on the opposite side of the module shell decreased just before the outlet. The entrance and exit effects were considered negligible if they only affected the flow directly downstream from the inlet and upstream of the outlet, and were contained to less than five percent of the module length. The entrance effects were negligible for some of the module geometries, even at higher flow rates. The entrance effects propagated past the acceptable entrance of the module in a few of the module geometries at higher flow rates. These affects were pronounced in 7SD, 13SD, 19SD and 19ES. Figure 5 shows the velocity magnitude taken from the same z-y plane of the 19SD near the inlet and outlet at r = 2.5 cm. The green line shows the velocity magnitude near the inlet ($\varphi = 5°$) and the blue line shows the velocity magnitude near the outlet ($\varphi = 175°$).

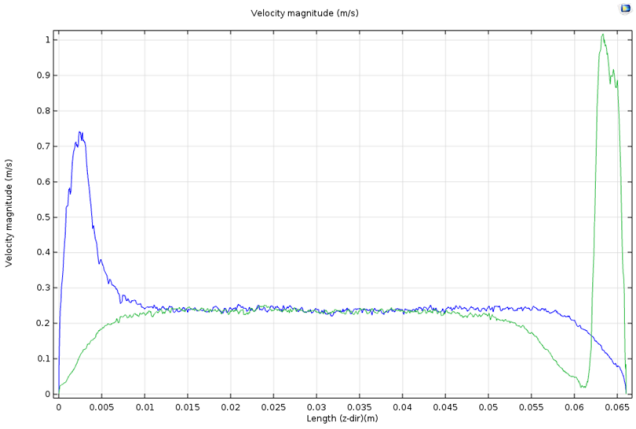


**Figure 5.** Entrance and exit effects in 19SD, at Q= 240 mL/min.

It was determined that the inlet and outlet effects could not be neglected for some of the modules at higher flow rates, therefore all modules had to include entrance and exit effects for comparison. The final geometry of the modules included a half cylinder shell with inlet and outlet, modeled with a symmetry boundary along the mid-plane of the module. Interestingly, the flux produced from these models was higher than the models that did not include the entrance and exit effects.

**Packing Configuration**

It is not feasible to place a membrane fiber in an exact position when fabricating hollow fiber membrane modules, so they are randomly packed. Therefore, the lab-tested modules were arbitrarily packed. Two packing density configurations were established for simulations to provide an upper and lower bound in order to account for the random spacing of the physical modules. Both configurations included the same area taken up by the membranes at each packing density. The flow on the shell side transports heat to the membrane surface. The permeate production is determined by the temperature difference across the membrane. The ES modules allow flow to be more evenly distributed than the SD modules at every flow rate, and therefore produce higher flux. The SD modules, in contrast, allow more channeling of the feed water through the area between the module wall and the center region where membranes are more closely packed. Since the fabricated modules are randomly packed, the flux produced by the modules should fall somewhere between the simulated model predictions for the two packing configurations.

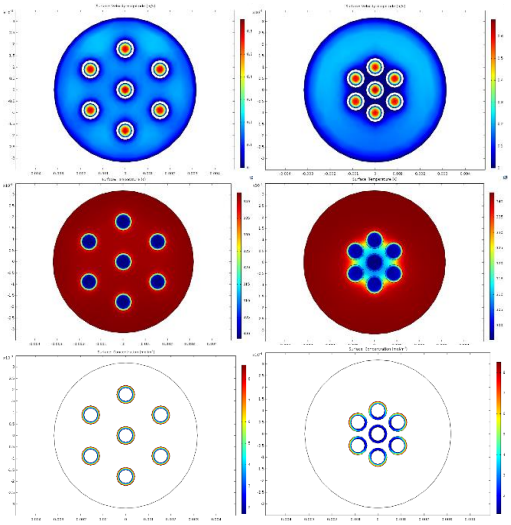

**Figure 6.** Effect of flow distribution on temperature profile and vapor concentration distribution

**Flow Rate**

Flow rate had a positive correlation with flux production for all of the module geometries.

The ES geometries produced a higher flux than their SD counterparts. The flow rate model predictions followed natural log trends. The simulations showed the greatest flux improvement from 30mL/min to 60mL/min. Additionally, the 13ES module had a higher flux increase at lower flow rates than the 13SD module. Figure 13 shows the predicted and tested flux for the modules containing thirteen membranes. The lab tested 13M modules followed a similar trend. Figure 14 shows the model predicted flux vs. TPC. The TPC for the ES models appeared to reach a plateau at 0.81 for the 13 membrane modules. While this parameter didn't improve much with increased flow rate for the ES models, the bulk and membrane temperatures in the feed and permeate domains continued to increase. The overall temperature increase provided a higher flux, even with similar temperature gradients, because the water vapor pressure increases exponentially with the temperature.

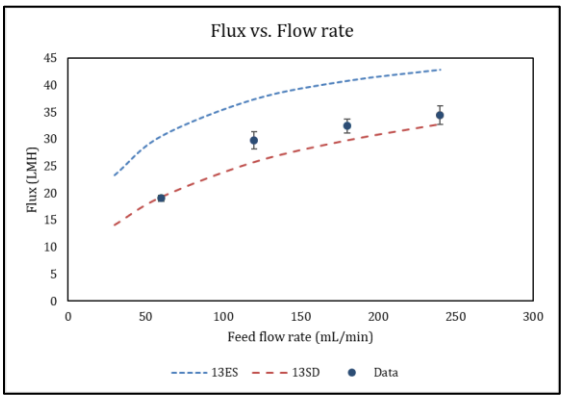


**Figure 7**. Flux predicted for 7-membrane configurations

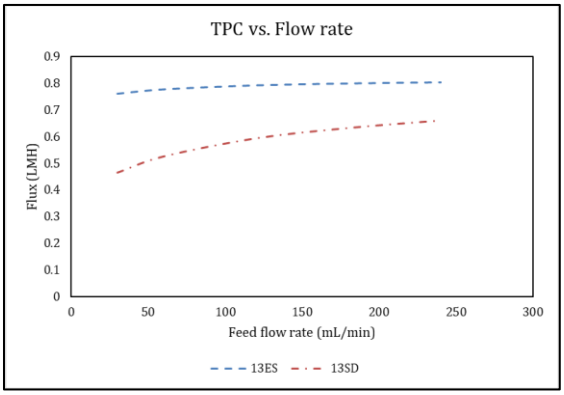


**Figure 8.** TPC vs. Flow rate for simulated modules containing 13 membranes.

**Packing Density**

The average velocity moving through the shell side of the module, as well as the surface area available for evaporation to occur, increased as packing density increased. Channeling became more severe as packing density increased, which lowered flux across the membrane. The SD models predicted a slightly decreasing flux as packing density increased (Figure 9). This is a result of the restricted velocity near the inner membrane walls on the shell side of the module due to channeling. Hot feed water preferentially flowed through the low-pressure regions around the membrane fibers, instead of the higher-pressure regions between the fibers. The unpredictable trend of the ES modules is a result of two counteracting effects of packing density. Increased velocity delivered heat at a higher rate through the shell side of the module, which had a positive impact on flux. The ES modules also experienced increased channeling as the distance between membrane fibers decreased with packing density. In These mechanisms can be seen in Figure 10.

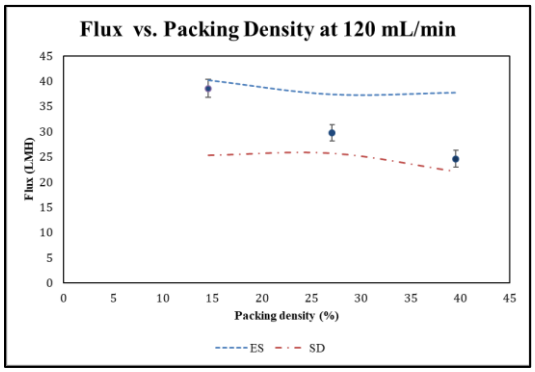


**Figure 9**. Flux vs. packing density for 13 modules simulations and lab tests.

Inspection of the fabricated lab-scale modules led to the observation that the modules containing seven membranes were generally more evenly distributed though the module cross-section than the modules with higher packing density. In contrast, the fibers were closer together in the 19M modules. This observation is in agreement with the relative flux of the lab-tested modules. The fabricated 7M modules performed similarly to the ES simulated modules, while the 19M modules performed similarly to the SD simulated modules. Figure 10 shows the temperature distribution of the various simulated module configurations and packing densities at 120 mL/min. The 19ES module experienced slightly less channeling, while the decreased shell-side area contributed to higher velocity, such that the bulk temperature for the shell remained higher than that of the 13ES simulation. The SD modules show an increased impact of flow channeling as the packing density increased. This phenomenon led to much lower flux production, as membranes placed in the center experienced lower flow.

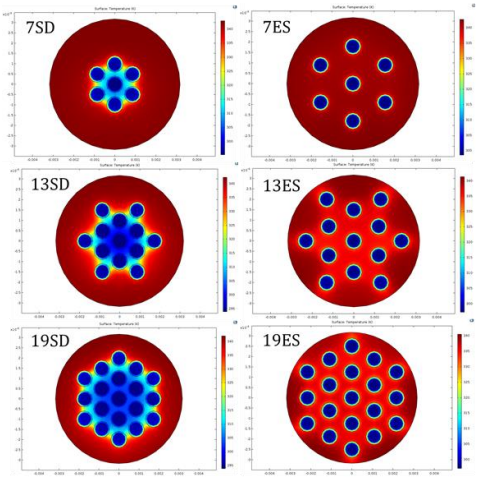


**Figure 10.** Effect of flow distribution on temperature.

The TPC of the modules increased slightly with packing density. Both configurations appeared to be reaching a plateau as packing density increased (Figure 11). The SD membranes were limited by their distribution and experienced higher temperature polarization. The ES membranes reached a plateau based on the MD process, which removes energy at the feed-membrane interface for evaporation and adds energy to the permeate-membrane interface as condensation occurs. The packing density of the modules adds a level of variability to predicting the flux of the modules. The distribution of membranes in the physical modules is not uniform, and cannot be easily predicted for a given packing density. The overall production of the module increases with packing density, while the flux, determined by the production per surface area, is variable.

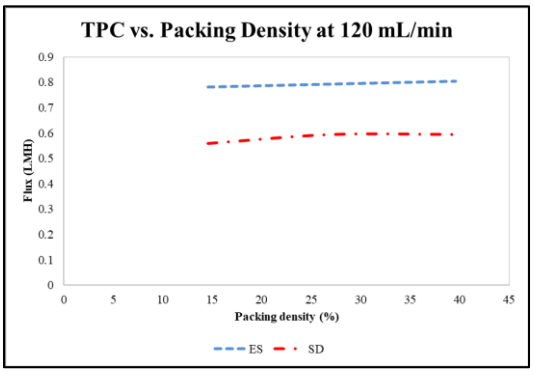


**Figure 11.** Packing density vs. TPC at 120 mL/min.

## Conclusions

The summarized project established a CFD model to investigate heat and mass transfer based on the physical processes involved in membrane distillation for a 3D multiple hollow-fiber membrane module. The CFD model allows determination of the membrane surface temperatures, as well as insight into mass and heat flow. The study investigated the effects of packing density and flow rate for different membrane configurations. Performance of the HDM in terms of water flux depends heavily on fiber packing configuration, packing density, and fluid flow rates. The main findings of the study were:

- Water flux is a strong function of the packing configuration. It doesn't follow a continuous trend with increasing packing density, and is highly impacted by channeling.
- For a set packing density, water flux increases with increasing flow rate. The increase of flux due to flow rate gradually levels out for each packing density and packing configuration. There is a direct correlation between the flow rate and bulk temperature as well as between flow rate and the temperature polarization coefficient (TPC).
- High packing density (≥50%) is necessary to predict the water flux of an actual module using CFD simulations.
- Significance of the entrance and exit effects should be evaluated for modeling large scale modules for water flux predictions. CFD simulations of lab scale modules with and without these effects showed discrepancy of up to 25%.
- Single fiber CFD simulations cannot predict module performance accurately due to difference in velocity distribution and evaporative surface area.

Overall, the CFD models can be incorporated to establish the best operating considerations for a specific DCMD system.

## References


1. Andrjesdóttir, Ó., Ong, C. L., Nabavi, M., Paredes, S., Khalil, A. S. G., Michel, B., Runyu, M. (1997). Membrane distillation. *Journal of Membrane Science*, *124*, 1–25.


## Acknowledgements


This work was supported by National Science Foundation award #IIA-1301346 to NM EPSCoR and its Osmotic Power Research Group.